Study and Optimization of Energy Absorption Characteristics of Windowed Multi-Cell Thin-Walled Conical Tube under the Axial Loading

Tieping Wei[1,2,*], Xiang Lin[1,2], Xingyang Zhou[1,2], Chao Kou[1,2] and Shoujin Zeng[1,2]

[1] Fujian Key Laboratory of Intelligent Machining Technology and Equipment, Fujian University of Technology, Fuzhou, 350118, China

[2] Department of Mechanical and Automotive Engineering, Fujian University of Technology, Fuzhou, 350118, China

Revista Internacional
Métodos numéricos
para cálculo y diseño en ingeniería
RIMNI
UNIVERSITAT POLITÈCNICA DE CATALUNYA BARCELONATECH
In cooperation with CIMNE

INFORMATION

Keywords:
Energy absorption characteristic
windowed multi-cell conical tube
prediction expression of the mean load
multi-objective optimization
LS-DYNA

DOI: 10.23967/j.rimni.2025.10.56507

SCIPEDIA Revista Internacional de Métodos Numéricos para Cálculo y Diseño en Ingeniería

RIMNI Revista Internacional Métodos numéricos para cálculo y diseño en ingeniería CIMNE

Study and Optimization of Energy Absorption Characteristics of Windowed Multi-Cell Thin-Walled Conical Tube under the Axial Loading

Tieping Wei[1,2,*], **Xiang Lin**[1,2], **Xingyang Zhou**[1,2], **Chao Kou**[1,2] **and Shoujin Zeng**[1,2]

[1]Fujian Key Laboratory of Intelligent Machining Technology and Equipment, Fujian University of Technology, Fuzhou, 350118, China

[2]Department of Mechanical and Automotive Engineering, Fujian University of Technology, Fuzhou, 350118, China

ABSTRACT

Conical tubes have attracted significant attention due to their more stable deformation mode and lower initial peak load compared to non-conical tubes under axial load. Firstly, based on LS-DYNA software and a multi-objective optimization algorithm, simulations of the conical tube structure under axial load were conducted to determine the optimal dimensions of the conical tube. Then, based on the optimal unicellular conical tube structure, the energy absorption characteristics of the windowed multi-cell conical tube structures with horizontal and vertical partitions and square holes were designed, and a predictive expression for the mean load was proposed based on the simulation data. Finally, the results show that the optimal dimensions of the mono-cell conical tube are $\varphi = 10°$ and $t = 1.29$ mm, while the optimal dimensions of the windowed multi-cell conical tube structure are four transverse split panels ($v = 4$), four vertical split panels ($n = 4$), and four holes ($k = 4$). Compared to the unicellular conical tube, the energy absorption efficiency of the windowed multi-cell conical tube has increased by 70.06%, while the initial peak load has decreased by 23.60%. Furthermore, both simulation and experimental results show that the predictive expression for the mean load of the windowed multi-cell conical tube exhibits good universality and reliability. The research results provide a new design concept for thin-walled conical tube energy absorption boxes.

OPEN ACCESS

Received: 24/07/2024

Accepted: 09/12/2024

Published: 20/04/2025

DOI
10.23967/j.rimni.2025.10.56507

Keywords:
Energy absorption characteristic
windowed multi-cell conical tube
prediction expression of the mean load
multi-objective optimization
LS-DYNA

1 Introduction

The impact kinetic energy generated by traffic accident collisions is primarily dissipated through the plastic deformation of the buffer device. Thin-walled circular tubes are widely utilized in the field of impact protection due to their advantages of being lightweight, high-strength, and having high energy absorption efficiency [1]. Compared to thin-walled circular tubes, thin-walled conical tubes with introduced conical angles have more stable deformation patterns and better energy absorption effects [2]. The main factors affecting the energy absorption characteristics of thin-walled circular

*Correspondence: Tieping Wei (wtp12312@sina.com).

tubes include material types [3–6], structure sizes [7–9] and loading conditions [10–12]. Therefore, the optimal design of thin-walled tube structure size has been researched deeply, especially the addition of partitions in the tube, which can improve stiffness and increase the induction of defects to weaken the initial peak load (F_{IPL}).

The addition of partitions can effectively improve the stiffness of tube fittings, thereby increasing the energy absorption capacity. The square tube can change its crushing mode and increase its crashworthiness level by adding transverse partitions [13]. Moreover, the horizontal partitions provide overall constraint to the conical tube, making the structure more stable and orderly under compression. This effect is greater than that of simply increasing the wall thickness on specific energy absorption (SEA) and F_{IPL} [14]. Jusuf et al. [15] utilized numerical simulations and experiments to investigate the energy absorption characteristics of double-layer multi-cell tubes under axial loading. The results indicated that adding partitions can effectively enhance energy absorption efficiency, but it may also exacerbate geometric compatibility issues [16]. In addition, combining the addition of transverse partition and filling with gradient honeycomb in the conical tube not only enhances the overall energy absorption, but also makes the deformation more stable. Therefore, it can be seen that the reasonable design of transverse and vertical partitions is beneficial to improve the energy absorption characteristics of conical tubes.

In terms of reducing F_{IPL} and improving the crushing deformation mode, opening holes and grooving [17,18] are the most direct and effective methods. Zhou et al. [19] and Song et al. [20] weakened FIPL by digging a rectangular hole in a square tube and effectively improved SEA. Based on the above, Song et al. [21] conducted a comparison and analysis of the energy absorption characteristics of equal mass between open square tubes and multi-cell square tubes. It is found that the multi-cell tube has a higher mean load (F_{ML}) than the open square tube, and also a larger F_{IPL}. Slotted conical tubes reduce F_{IPL} by sacrificing energy absorption capability, thereby improving overall energy absorption efficiency [22]. Additionally, hole opening and the addition of grooving can reduce F_{IPL}, and the energy absorption efficiency of the open conical tube is higher than that of slotted conical tubes, although F_{IPL} is higher than that of slotted conical tubes [8]. At the same time, Nikkhah et al. [23] found that squares and rectangles were the best shapes for opening holes. Further, the opening and grooving will also affect the crushing deformation mode of the structure. Song et al. [20] found that F_{IPL} of a perforated square tube decreased significantly under inclined load conditions, but its instability resistance and overall energy absorption capacity both decreased. However, Gupta et al. [24,25] found that the introduction of a circular hole on the surface of a circular tube can avoid overall buckling when the slenderness ratio is large. To sum up, the energy absorption effect of thin-walled tube can be effectively improved by reasonable design of opening and grooving. Many scholars have conducted further research on the energy absorption mechanisms of thin-walled tubes [26–29]. The energy absorption mechanism of conical tubes is primarily based on the theoretical foundations of circular tubes. Postlethwaite et al. [27] proposed a theoretical formula for average load applicable to conical tubes based on Alexander's method [28]. Mamalis et al. [29] developed a theoretical model for conical tubes with angles of 5°, 10° and 14.35°, effectively predicting the impact of cone angle and wall thickness on energy absorption characteristics. Further, Zhang et al. [30] introduced a novel load prediction formula for multi-cell square tubes by decomposing the cross-section into angular, cruciform, and T-shaped elements, followed by validation.

In conclusion, there is currently limited research on conical tube structures that simultaneously consider enhancing energy absorption capacity and reducing F_{IPL}. Adding horizontal and vertical partitions and openings can improve the energy absorption efficiency of thin-walled tubes while maintaining stable deformation modes. The windowed multi-cell conical structure, which is composed

of two or more combined structures, has significant research value. This paper proposes windowed multi-cell conical tube (WMCT) structure and investigates its energy absorption characteristics and crushing mechanism under axial loading, deriving a theoretical formula for the average load. Firstly, the unicellular conical tube (UCT) with inclination angle of 5°∼10° and wall thickness of 1∼2 mm [31] is simulated under the axial load to analyze the influence of inclination angle and wall thickness on energy absorption characteristics and deformation mode. The optimal unicellular conical tube (O UCT) is obtained by multi-objective optimization method. On this basis, the energy absorption mechanism and characteristics of WMCT are studied by adding transverse and vertical partitions and opening holes. Finally, the prediction expression of WMCT's F_{ML} is derived and verified by the experiment.

2 Finite Element Model for UCT

2.1 Finite Element Model

(1) Structural dimension parameters

Considering the energy absorption characteristics [32] of UCT with a wide range of inclined angles and the physical size of the energy absorption box [33], the range values of the height L, the diameter D of the big end, the conical inclination φ and the wall thickness t of the energy absorption box are determined, as shown in Table 1. In addition, the corresponding diagram is shown in Fig. 1.

Table 1: Structural dimension parameters of UCT

L/mm	D/mm	φ/°	t/mm
200	90	5∼10	1∼2

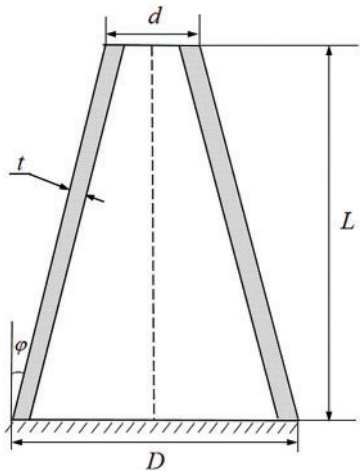

Figure 1: Schematic diagram of UCT

(2) Material property

The material selected is A6061-T4, and its elastic-plastic behavior is isotropic. As shown in Fig. 2, uniaxial tensile test is carried out on A6061-T4 specimen according to the requirements of GB/T 228-2010 and GB/T 2975-1998. The stress-strain relationship curve (as shown in Fig. 3) and performance parameters (as shown in Table 2) are obtained.

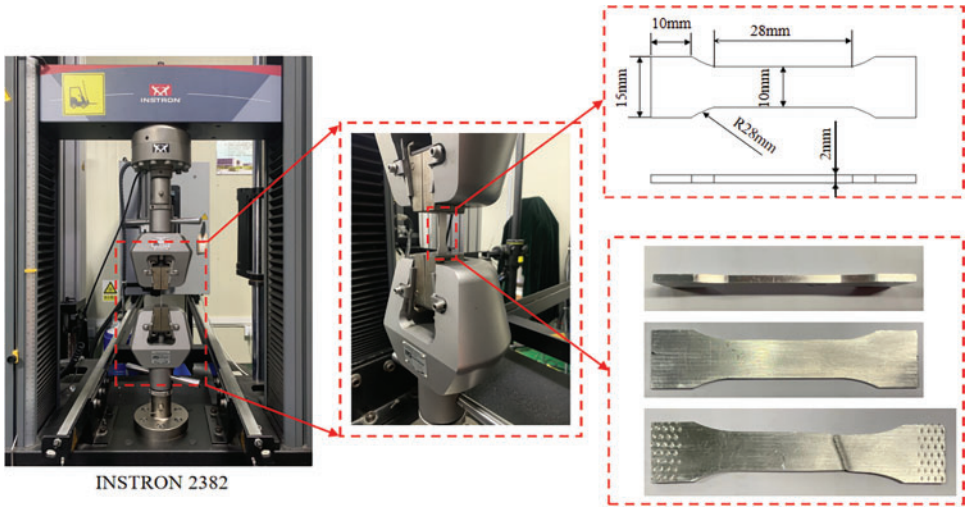

Figure 2: The tensile test for the A6061-T4 specimen

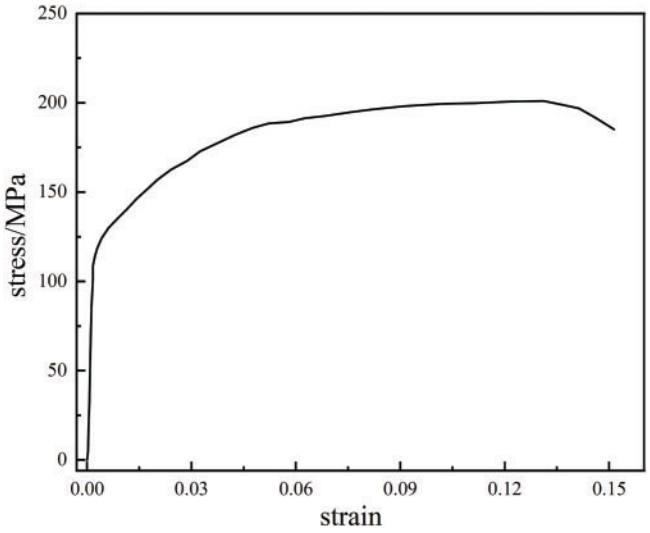

Figure 3: The stress-strain curve for the A6061-T4 specimen

Table 2: Material property of A6061-T4

Density ρ/(kg·m^{-3})	Elastic modulus E/MPa	Yield strength σ_f/MPa	Poisson ratio v
2700	68,900	128	0.3

(3) The parameters of the finite element model

ANSYS/LS-DYNA is used for numerical calculation in this paper. The model includes the conical tube, punch and fixed panel. The static and dynamic friction coefficients between the thin-walled tube and the punch, and between the thin-walled tube and the fixed panel are all set to 0.2. The contact mode between the three components is set to “Automatic single-surface contact”.

During the compression process, the panel is fixed while the punch compresses downward along the axis of the conical tube at a speed set to $V = 1$ m/s, as shown in Fig. 4. The deformation stiffness of the punch and the fixed panel is much larger than that of the thin-walled tube fitting. Therefore, the punch and the fixed panel in the model are assumed to be rigid plates, and the material model Mat20# is selected. The thin-walled conical tube has a small wall thickness and uses Belytschko-Tsay shell elements. This shell element is characterized by high computational efficiency and accuracy. The Belytschko-Tsay four-node thin shell element is a first-order linear element that employs reduced integration in the plane of the element. The material model selected is Mate24#.

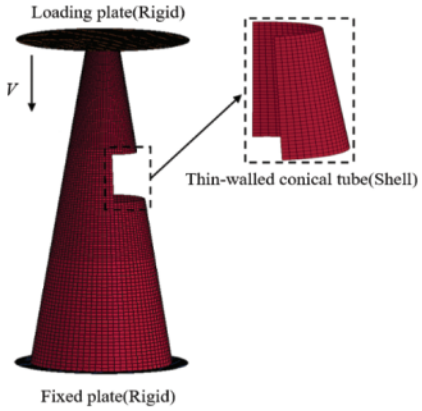

Figure 4: The finite element model of UCT

2.2 Determination of Mesh Size

The mesh size has an important influence on the accuracy of simulation results and calculation cost. In this paper, the different mesh sizes from 1.0 to 3.0 mm and an inclination angle of 10° for UCT are simulated and analyzed. As shown in Fig. 5, the calculation time and total energy absorption (EA) of different grids are analyzed and it is found that EA tended to converge when the mesh size less than 1.5 mm. At the same time, when the mesh size is 1 mm, the calculation time is much longer than that of 1.5 mm. Therefore, considering the calculation cost and accuracy requirements, the mesh size of 1.5 mm is more suitable.

2.3 Verification for the Finite Element Model

In order to verify the reliability of the finite element model, a finite element model analysis consistent with that in the literature [34] is conducted, and the load-displacement curve of the simulation results is compared with the deformation mode, as shown in Figs. 6 and 7. As shown in the figures, when the compression amount reaches 80 mm, the average load obtained from the experiment is 23.0 kN, while the simulation result presented in this paper is 22.3 kN, with a difference of 3.04%. Furthermore, both have the same number of folds, and their deformation modes are consistent, each exhibiting a triangular diamond pattern. The consistency of these results demonstrates the accuracy and reliability of the finite element model presented in this paper.

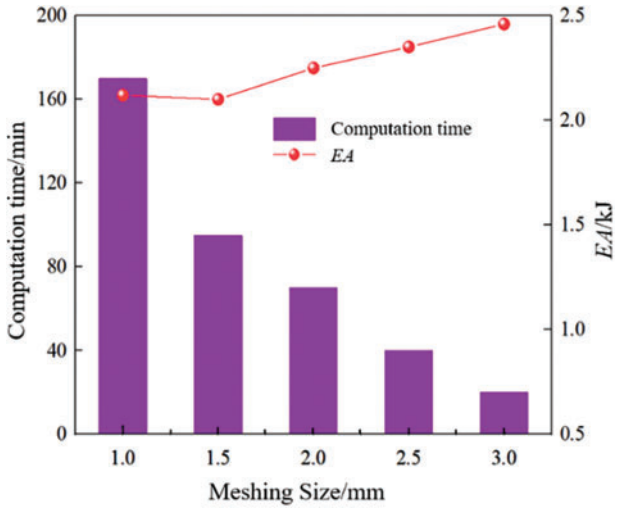

Figure 5: The grid sensitivity analysis

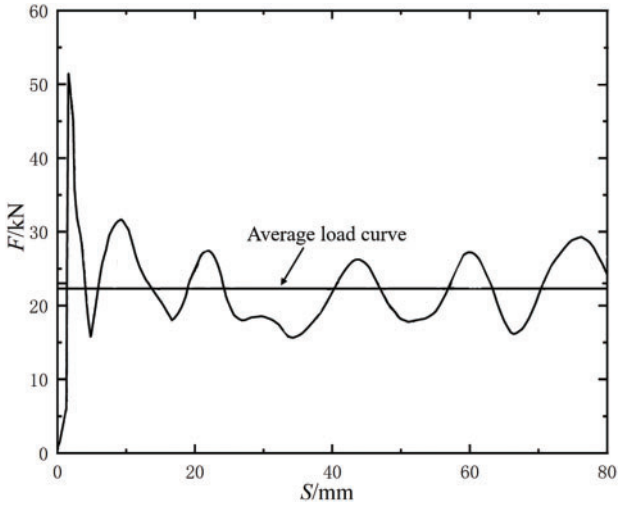

Figure 6: The force-displacement curve

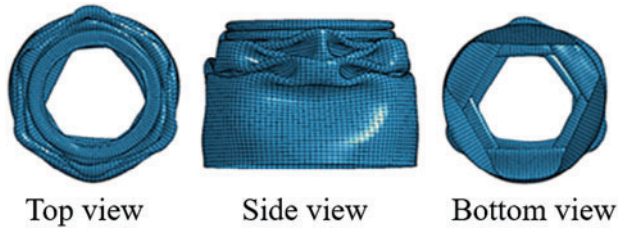

Figure 7: The compressive deformation mode

3 Optimization Design of WMCT

3.1 Multi-Objective Optimization of UCT

3.1.1 Multi-Objective Optimization Function

SEA and F_{IPL} are two important indexes used to evaluate the crashworthiness of structures. Combined with various variable parameters in Table 1, the multi-objective optimization problem of UCT can be described as finding the maximum values of *SEA* and $-F_{\mathrm{IPL}}$ in the design region. Therefore, the multi-objective optimization problem of UCT is defined as follows:

$$\begin{cases} \text{Max} & SEA = f(t,\varphi); \\ \text{Max} & -F_{\mathrm{IPL}} = -f(t,\varphi); \\ \text{s.t.} & 1\,\text{mm} \le t \le 2\,\text{mm} \\ & 5^\circ \le \varphi \le 10^\circ \end{cases} \tag{1}$$

3.1.2 Proxy Model Reliability Verification

Firstly, in order to take into account the accuracy of the Kriging proxy model and the simplicity of calculation, ten sample points are selected in the design region using the optimal Latin hypervertical method. The structural dimension and simulation results are shown in Table 3. Secondly, the calculation results of ten sample points are extracted to fit the Kriging proxy model, and the determination coefficient (R^2) and root mean square (RMSE) are used to evaluate the accuracy of the constructed proxy model. In addition, because the proxy model constructed by Kriging method covers ten sample points, it cannot reach the test effect [35] if the ten sample points used to construct the agent model are used to evaluate the accuracy of the model. Therefore, three sample points are needed to be generated to evaluate the accuracy of the proxy model as shown in Tables 4 and 5 that are the evaluation results of the proxy model and the comparison of accuracy between the finite element model and Kriging model, respectively. Finally, it shows that the model constructed by Kriging model has high precision, and the relative error of the three groups of data is within 4%, which indicates that the proxy model is accurate and reliable.

Table 3: Structural dimension design and simulation results of UCT

No.	t/mm	φ/°	F_{IPL}/kN	SEA/(kJ∗kg^{-1})
1	1.78	5.56	39.18	19.06
2	1.56	8.33	21.47	17.81
3	1.44	6.67	27.25	17.76
4	1.22	9.44	13.30	16.23
5	1.67	10.0	17.79	19.35
6	1.0	6.11	19.57	14.35
7	1.89	7.22	33.74	20.75
8	1.33	5.0	30.96	18.01
9	1.11	7.78	15.94	15.37
10	2.0	8.89	28.58	21.33

Table 4: Accuracy evaluation of surrogate model for UCT

Specimen	Evaluation index	R^2	RMSE
O UCT	F_{IPL}	0.9912	0.0290
	SEA	0.9754	0.0476

Table 5: Comparison of results between the precision of finite element model and Kriging model

No.	t/mm	φ/°	F_{IPL}/kN			SEA/(kJ∗kg^{-1})		
			FEA	Kriging	Error/%	FEA	Kriging	Error/%
11	1.09	5.34	23.90	23.78	0.50	14.79	15.27	−3.24
12	1.50	6.23	30.68	30.87	−0.62	17.69	17.76	−0.40
13	1.72	9.94	19.56	18.94	3.17	20.50	20.13	1.80

3.1.3 Optimization Results

The essence of multi-objective optimization design of UCT is to find the best balance between energy absorption efficiency and deformation mode stability through the optimal matching of φ and t, which is ultimately the stiffness design. As we known, Pareto front provides a set of optimal solutions, which provides guidance for engineering design.

The two-dimensional diagram of UCT multi-objective optimization is as shown in Fig. 8. Since F_{IPL} and SEA are two conflicting optimization objectives, increasing SEA directly leads to a rapid increase in F_{IPL}. Therefore, take the F_{IPL} negative, and set the maximum value of $-F_{IPL}$ as the expectation. As can be seen from Fig. 8, SEA is positively correlated with $-F_{IPL}$, that is, the increase of SEA will lead to the increase of $-F_{IPL}$.

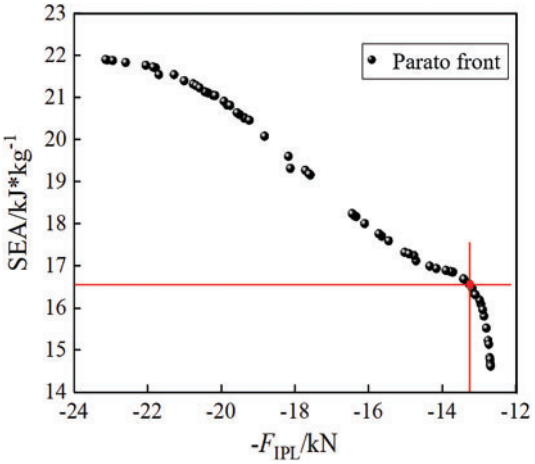

Figure 8: Pareto front of UCT

In order to specifically analyze the characteristics of the optimal solution, two points (SEA (max) and $-F_{IPL}$ (max)) on the edge of Pareto front curve and UCT with comprehensive optimal solution

(O UCT for short) are selected, which are summarized in Table 6. It can be seen that all the conical inclination angles are close to 10°, indicating that the larger conical inclination angle is conducive to the stability and crashworthiness, and t corresponding to SEA (max) is 1.91 mm. In addition, the larger thickness is able to increases the stiffness and energy absorption area of the structure, and improves the energy absorption efficiency, but F_{IPL} also increases sharply. At the same time, t corresponding to $-F_{\mathrm{IPL}}$ (max) is 1 mm, which will reduce the stiffness and energy absorption area of the structure, resulting in the reduction of F_{IPL}, but the energy absorption efficiency of the structure will also decline. However, $\varphi = 10°$ and $t = 1.29$ mm of O UCT are able to ensure the energy absorption efficiency and reduce F_{IPL}. Therefore, O UCT is an integrated optimal solution of two conflicting performance indicators.

Table 6: The data comparison among SEA (max), $-F_{\mathrm{IPL}}$ (max) and O UCT

	$\lvert -F_{\mathrm{IPL}}\rvert$/kN	SEA/(kJ∗kg^{-1})	Optimal solution	
			φ/°	t/mm
SEA (max)	23.14	21.90	9.97	1.91
O UCT	13.26	16.57	10.00	1.29
$-F_{\mathrm{IPL}}$ (max)	12.69	14.62	9.36	1.00

Furthermore, comparison and verification of multi-objective optimization values and simulation values are shown in Table 7. It can be seen that the relative error of F_{IPL} and SEA are both less than 2%, which verifies the reliability of the simulation calculation.

Table 7: Comparison of multi-objective optimization values with simulation value

	Multi-objective optimization values	Simulation value	Relative error/%
$\lvert -F_{\mathrm{IPL}}\rvert$/kN	13.26	13.07	1.45
SEA/(kJ∗kg^{-1})	16.57	16.73	−0.96

3.2 Multi-Objective Optimization of WMCT

WMCT is designed based on the optimization results of the O UCT. The addition of horizontal and vertical partitions, on the basis of traditional conical tubes, enhances energy absorption stability and improves SEA, but increase F_{IPL} [13–15]. As we known, induction holes can be dug to induce the conical tube collapse deformation [19–21], which can reduce F_{IPL}.

3.2.1 Structure Design of WMCT

Based on the O UCT ($\varphi = 10°$, $t = 1.29$ mm), the square hole [23–26] is designed for the WMCT, as shown in Fig. 9. It can be seen that the transverse partition board is arranged equidistant from the small end to the big end successively, while the start positions of square holes are arranged equidistant from the small end (above the transverse partition) to the large end. Additionally, based on the dimensions of the energy-absorbing box structure, the interaction among the thickness of the partition walls, the number of horizontal and vertical partitions, and the number of square hole layers was comprehensively considered. The determined size parameters are shown in Table 8.

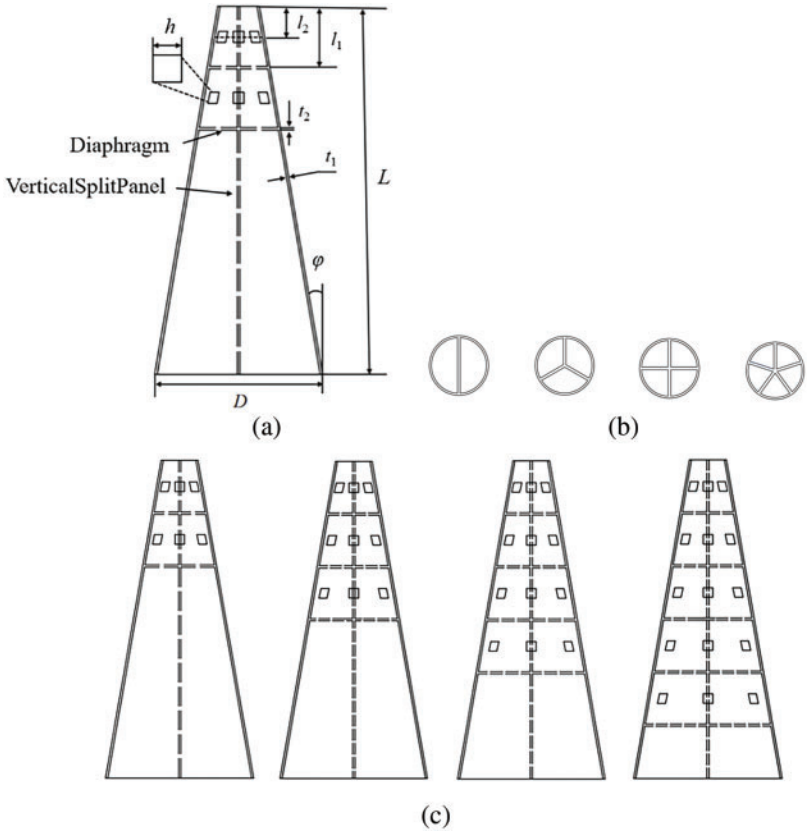

Figure 9: WMCT schematic diagram: (a) Schematic diagram of tube; (b) Distribution of vertical partitions; (c) Distribution of the diaphragms and square holes

Table 8: The structural size of WMCT

Name	Units	Value
Overall height/L	mm	200
Conical inclination angle/φ	°	10
Big end diameter/D	mm	90
Partition spacing/l_1	mm	33.3
Spacing between holes and partitions/l_2	mm	16.7
Square hole side length/h	mm	6
Outer tube wall thickness/t_1	mm	1.29
Partition wall thickness/t_2	mm	1∼2
Number of square holes/k	layer	2∼5
Number of transverse partitions/m		2∼5
Number of vertical partitions/n		2∼5

3.2.2 Multi-Objective Optimization Model for WMCT

In order to obtain the best energy absorption characteristics of WMCT, the maximum points of SEA and $-F_{IPL}$ in the design region are selected for the objective function. The main influencing factors of the energy absorption characteristics of WMCT include m, n, t_2 and k. Therefore, the multi-objective optimization mathematical model of WMCT is as follows:

$$\begin{cases} \text{Max} & SEA = f(t_2, k, m, n); \\ \text{Min} & F_{\text{IPL}} = f(t_2, k, m, n); \\ \text{s.t.} & 1\,\text{mm} \le t_2 \le 2\,\text{mm} \\ & 2 \le k \le 5 \\ & 2 \le m \le 5 \\ & 2 \le n \le 5 \end{cases} \tag{2}$$

3.2.3 Proxy Model Reliability Verification

The optimal design scheme of WMCT is determined as L_{16} (4^5), as shown in Table 9. A, B, C (empty column), D and E correspond to m, n, k and t_2, respectively. The design scheme and simulation analysis results are shown in Table 10.

Table 9: Factors and levels of the orthogonal test L_{16} (4^5)

Level	A	B	C	D	E
1	2	2	–	2	1
2	3	3	–	3	1.33
3	4	4	–	4	1.66
4	5	5	–	5	2

Table 10: The orthogonal test scheme and analysis results

No.	Column number					F_{IPL}/kN	SEA/(kJ∗kg^{-1})
	A	B	C (empty column)	D	E		
1	2	2	1	2	1	6.79	18.57
2	2	3	2	3	1.33	9.62	24.10
3	2	4	3	4	1.66	10.03	27.29
4	2	5	4	5	2	13.71	28.59
5	3	2	2	4	2	8.60	19.24
6	3	3	1	5	1.66	9.28	24.03
7	3	4	4	2	1.33	11.07	26.51
8	3	5	3	3	1	12.22	26.92
9	4	2	3	5	1.33	7.52	18.62
10	4	3	4	4	1	8.91	22.28
11	4	4	1	3	2	11.34	29.37
12	4	5	2	2	1.66	13.59	29.73

(Continued)

Table 10 (continued)

No.	Column number					F_{IPL}/kN	SEA/(kJ∗kg^{-1})
	A	B	C (empty column)	D	E		
13	5	2	4	3	1.66	7.87	18.22
14	5	3	3	2	2	11.18	26.83
15	5	4	2	5	1	9.38	24.20
16	5	5	1	4	1.33	12.61	27.82

Four additional sample points (No. 17–20) are established. Then, R^2 and RMSE are used to evaluate the accuracy of the proxy model, as shown in Tables 11 and 12. The results show that the accuracy of the model constructed by Kriging model is high, and the relative error of the three groups of comparison verification is less than 5%, which indicates that the proxy model is accurate and reliable.

Table 11: Accuracy evaluation of proxy model for WMCT

Specimen	Evaluation index	R^2	RMSE
WMCT	F_{IPL}	0.9683	0.0695
	SEA	0.9800	0.0653

Table 12: Precision comparison between finite element model and Kriging model

No.	m	n	k	t_2/mm	F_{IPL}/kN			SEA/(kJ∗kg^{-1})		
					FEA	Kriging	Relative error/%	FEA	Kriging	Relative error/%
17	3	2	3	1.33	7.63	7.06	3.82	18.61	18.28	1.81
18	3	3	4	1.66	10.03	9.57	4.41	23.31	22.59	3.18
19	3	4	2	2	11.84	12.09	−2.07	30.68	29.46	4.14
20	5	2	5	1.66	8.19	7.96	2.89	18.23	18.92	−3.64

3.2.4 Optimization Results

SEA (max) and $-F_{IPL}$ (max) on the edge of Pareto front curve are selected for comparison and analysis with the optimal solution of the windowed multi-cell conical tube (O WMCT), as shown in Fig. 10 and Table 13. From the table, it can be observed that when the number of horizontal and vertical partitions and the wall thickness of the partition of SEA (max) are both large values, and k is the minimum value, increasing t_2 is conducive to improving the overall stiffness, thus increasing the energy absorption. At the same time, F_{IPL} increases sharply, and $-F_{IPL}$ (max) corresponds to a small m, n and t_2, and $k = 3$. In this case, reducing t_2 helps to reduce the overall stiffness. Therefore, the increase of k effectively reduces F_{IPL}, but SEA also decreases. m, n, t_2 and k are all equal to 4, which not only ensures the structure has sufficient stiffness and large SEA, but also obtains small F_{IPL}. In summary, O WMCT has better comprehensive energy absorption characteristics.

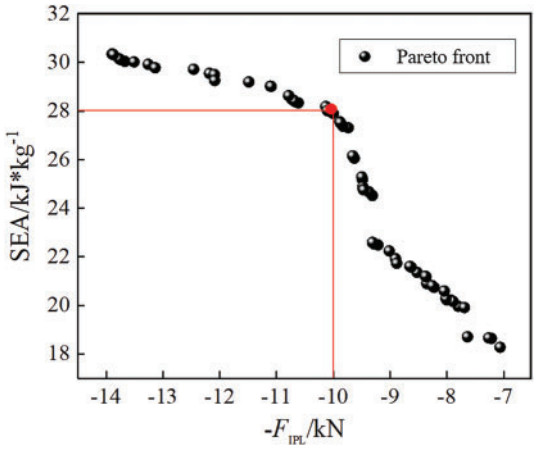

Figure 10: Pareto front of WMCT

Table 13: Data of *SEA* (max), $-F_{IPL}$ (max) and O WMCT

	$\lvert -F_{IPL}\rvert$/kN	*SEA*/(kJ∗kg^{-1})	Optimal solution			
			m	n	k	t_2/mm
SEA (max)	13.90	30.35	4	5	2	1.93
O WMCT	10.13	28.18	4	4	4	1.95
$-F_{IPL}$ (max)	7.06	18.28	3	2	3	1.21

Furthermore, the results of multi-objective optimization and simulation are compared in Table 14. It can be seen that the corresponding relative errors between F_{IPL} and *SEA* are both less than 5%, which verifies the reliability of the simulation calculation.

Table 14: Comparison between theoretical optimization and simulation

	Theoretical optimization	Simulation	Relative error/%
$\lvert -F_{IPL}\rvert$/kN	10.13	10.36	−2.22
SEA/(kJ∗kg^{-1})	28.18	28.43	−0.87

4 Analysis and Discussion of Optimization Results

In order to further explore the energy absorption advantages of WMCT, the energy absorption characteristics of O WMCT and O UCT are compared and analyzed. Fig. 11 shows the comparison of load-displacement curves between O WMCT and O UCT, while Table 15 shows the comparison of energy absorption characteristics. It can be seen that F_{IPL} of O WMCT is 23.60% smaller than that of O UCT, while *SEA* and *EA* of O WMCT increase by 70.06% and 90.66%, respectively. This is because the addition of square holes can reduce the local stiffness at the collision end. Furthermore, the addition of transverse and vertical partitions is able to enhance the stiffness and increases *EA*. However, due to the interaction between transverse and vertical partitions, O UCT has a more regular deformation

mode than O WMCT. In addition, Fig. 12 shows deformation modes for O WMCT and O UCT at 0.04, 0.08, 0.12 and 0.16 s. It can be seen that O WMCT exhibits a diamond pattern and folds in an orderly layer by layer manner due to the interaction between the partitions and the hole. It is a non-axisymmetric deformation mode as shown in Fig. 12a, while Fig. 12b illustrates that O UCT starts bending and collapsing from the top, forming a relatively stable diamond pattern with five folds.

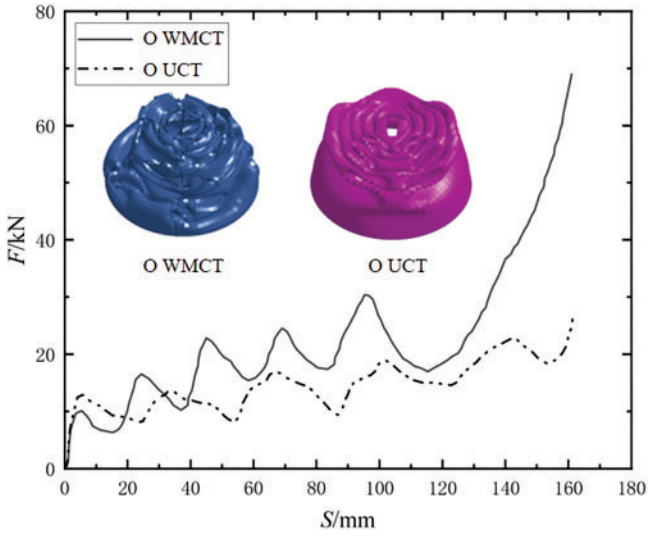

Figure 11: Load-displacement curves of O WMCT and O UCT

Table 15: Comparison of energy absorption characteristics between O WMCT and O UCT

	O WMCT	O UCT	Discrepancy/%
F_{IPL}/kN	10.13	13.26	−23.60
SEA/(kJ∗kg^{-1})	28.18	16.57	70.06
EA/kJ	5.51	2.89	90.66

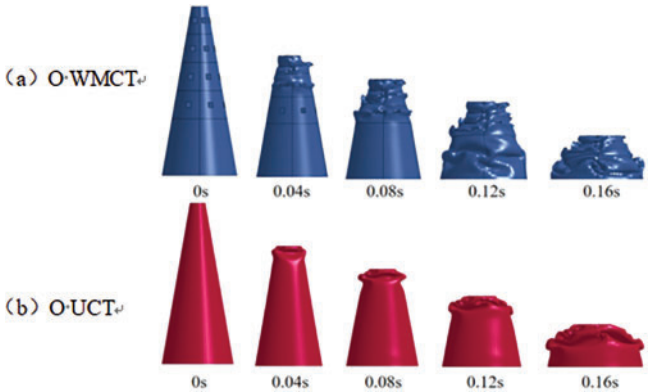

Figure 12: Compression deformation of O WMCT and O UCT

5 Prediction Expression for F_{ML}

5.1 Expression Derivation

In order to derive the prediction expression for F_{ML} of WMCT, 28 sets of data are designed and simulated, as shown in Table 16. Based on the expression [31] for F_{ML} of UCT (as shown in Eq. (3)), and considering the interaction of the four factors of WMCT, the approximate functional relationship between the response value ($\widehat{y}$) and the four factors x_j ($j = 1, 2, \ldots, m$) is derived by the multiple linear regression equation and the least square method, as shown in Eq. (4).

$$\overline{P} = 6\mathrm{Y}{t_1}^{1.5}\left(d^{0.5} + 0.95{t_1}^{0.5}\tan\varphi\right) \tag{3}$$

$$\widehat{y} = a + b_1x_1 + b_2x_2 + \cdots + b_mx_m \tag{4}$$

where Y is the average yield stress of the material, d is the diameter of the small end.

Table 16: The data of F_{ML}

No.	Column number				F_{ML}/kN
	m	n	k	t_2	
1	2	2	2	1	8.51
2	2	3	3	1.33	11.98
3	2	4	4	1.66	18.07
4	2	5	5	2	24.21
5	3	2	4	2	12.53
6	3	3	5	1.66	14.72
7	3	4	2	1.33	16.43
8	3	5	3	1	16.41
9	4	2	5	1.33	10.62
10	4	3	4	1	12.38
11	4	4	3	2	24.44
12	4	5	2	1.66	25.75
13	5	2	3	1.66	13.37
14	5	3	2	2	21.65
15	5	4	5	1	15.27
16	5	5	4	1.33	22.49
17	3	2	3	1.33	9.98
18	3	3	4	1.66	15.02
19	3	4	2	2	23.67
20	5	2	5	1.66	12.75
21	2	2	3	2	12.71
22	4	3	3	1.66	16.75
23	1	2	2	2	11.88
24	1	4	2	1.66	16.37
25	1	3	4	1.33	10.84
26	0	2	2	2	10.62
27	0	3	2	2	15.07
28	0	2	4	2	9.71

Therefore, the empirical formula of F_{ML} is as follows:

$$y = \lambda \overline{P}\,(a + b_1 x_1 + b_2 x_2 + \cdots + b_m x_m) \tag{5}$$

Set $x_1 = m$, $x_2 = n$, $x_3 = k$, $x_4 = t_2$, $x_5 = mn$, $x_6 = mk$, $x_7 = mt_2$, $x_8 = nk$, $x_9 = nt_2$, $x_{10} = kt_2$, $x_{11} = mnk$, $x_{12} = mnt_2$, $x_{13} = mkt_2$, $x_{14} = nkt_2$ and $x_{15} = mnkt_2$, and insert the data of the Table 16 into the argument variables x_1, x_2, …, and x_{15}, then x_{1i}, x_{2i}, …, x_{10i} and y_i ($i = 1, 2, \ldots, n$) are obtained. Finally, x_{1i}, x_{2i}, …, and x_{15i} are substituted into Eq. (4), and the calculated value of $\widehat{y}_i$ is obtained.

The simulation data in Table 16 are substituted into Eq. (5), and the coefficients obtained are substituted into Eq. (4) to obtain the multiple linear regression Eq. (6). Furthermore, R^2 and significance p are equal to 0.997 and 0.001, respectively, which indicates that the fitting of Eq. (6) meets the statistical requirements.

$$\begin{aligned}\widehat{y} = {} & 8.573 - 1.080x_1 - 4.290x_2 - 0.933x_3 \\ & - 1.980x_4 + 1.068x_5 + 0.222x_6 + 0.570x_7 \\ & + 0.947x_8 + 4.019x_9 + 0.060x_{10} - 0.201x_{11} \\ & - 0.312x_{12} - 0.039x_{13} - 0.432x_{14} + 0.069x_{15}\end{aligned} \tag{6}$$

The data are substituted into Eq. (5), the solution $\lambda = 0.236$ is obtained. Then, the prediction expression for F_{ML} of WMCT is as follows:

$$\begin{aligned}\widehat{y} = {} & 0.236(8.573 - 1.080x_1 - 4.290x_2 \\ & - 0.933x_3 - 1.980x_4 + 1.068x_5 + 0.222x_6 \\ & + 0.570x_7 + 0.947x_8 + 4.019x_9 + 0.060x_{10} \\ & - 0.201x_{11} - 0.312x_{12} - 0.039x_{13} - 0.432x_{14} \\ & + 0.069x_{15})\overline{P}\end{aligned} \tag{7}$$

5.2 Universality Verification

To verify the general applicability of the prediction expression, six additional sets of simulation data (No. 29–34) are designed and calculated, as shown in Table 17. By comparing the simulation data with the theory, it is found that the relative error between the simulation and the theory of F_{IPL} and SEA are both less than 10%, which indicates that the prediction expression has good general applicability.

Table 17: Comparing simulation with the predicted expression

No.	m	n	k	t_2/mm	F_{ML}/kN		Relative error/%
					FEA	Theory	
29	3	2	2	2	13.53	13.78	−1.81
30	2	3	2	2	17.89	17.35	3.11
31	1	2	3	2	10.66	11.18	−4.65
32	0	0	2	0	7.15	6.71	6.56

(Continued)

Table 17 (continued)

No.	m	n	k	t_2/mm	F_{ML}/kN		Relative error/%
					FEA	Theory	
33	0	0	3	0	5.35	5.77	−7.28
34	0	0	4	0	5.24	4.84	8.26

5.3 Experimental Verification

In order to further verify the reliability and validity of the prediction expression, the calculated results are verified by experiments. Considering the difficulty of specimen processing, three groups of specimens (No. 32−34) without transverse and vertical partitions are selected for verification of the test model, as shown in Fig. 13. In addition, the tests were conducted using a DNS300 electronic universal testing machine, with the punch compression speed set at 5 mm/min, as shown Fig. 14.

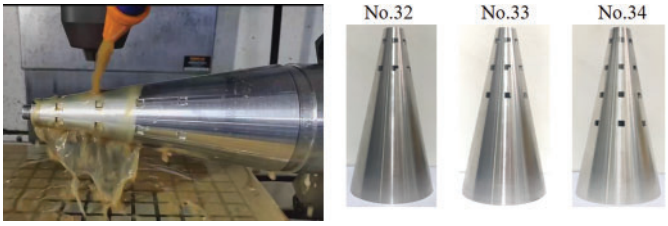

Figure 13: Specimen processing

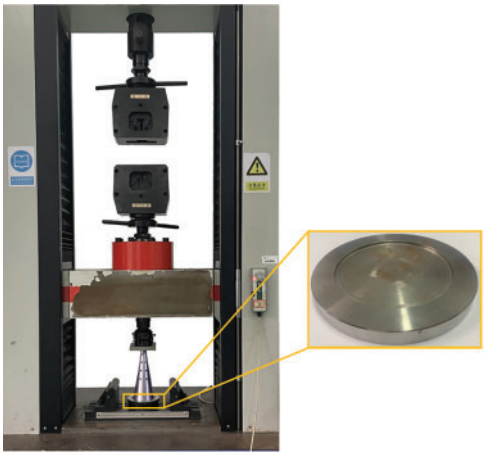

Figure 14: The quasi-static compression test equipment

The load-displacement curves of test and simulation for No. 32−34 specimens are showed in Fig. 15. As shown in the figure, the experiment and the simulation have the same change trend on the whole, and the consistency is good. However, the coincidence of peak and valley values is misplaced, which may be caused by the factors such as the vibration of the actual environment and the accuracy of the testing machine itself during the experiment, which does not affect the reliability of the verification simulation model. In addition, the deformation modes of the test and the simulation are shown at

different times, as shown in Fig. 16. It can be seen that the three specimens all formed folds at the square hole position, which is consistent with the deformation mode of simulation analysis. Further, Table 18 shows the comparison of test values with simulation values and theoretical values. As can be seen from the table, the maximum relative error is 3.78%, and the maximum relative error between the test and the theory is 8.85%. In conclusion, the experiment verifies the accuracy and reliability of the prediction expression of WMCT, and further verifies that WMCT has better energy absorption characteristics than UCT.

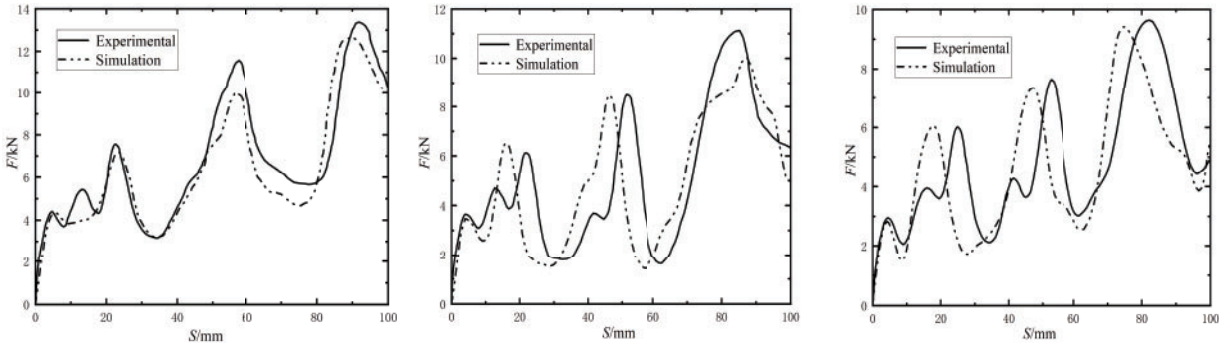

(a) No. 32 specimen (b) No. 33 specimen (c) No. 34 specimen

Figure 15: Load-displacement curves of test and simulation

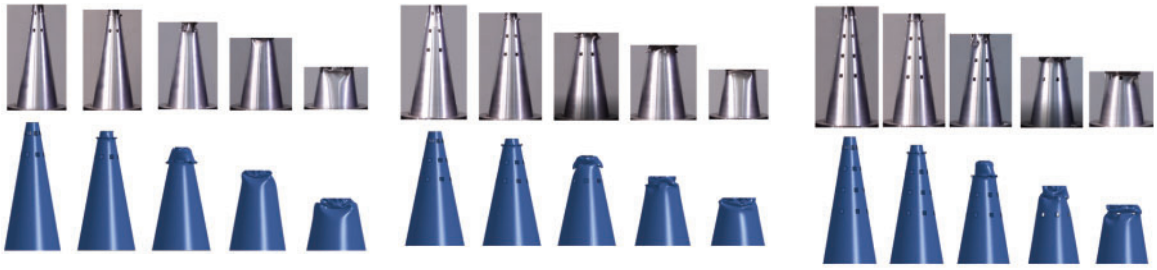

(a) No. 32 specimen (b) No. 33 specimen (c) No. 33 specimen

Figure 16: Deformation modes of test and simulation at different time

Table 18: Comparison of test with simulation and theory

No.	F_{ML}/kN			The relative error between the test and the simulation/%	The relative error between the test and theory/%
	Test	Simulation	Theory		
32	7.23	7.15	6.71	1.11	7.19
33	5.56	5.35	5.77	3.78	−3.78
34	5.31	5.24	4.84	1.32	8.85

6 Conclusions

In this paper, UCT with the best energy absorption characteristics is obtained by multi-objective optimization. On the above basis, WMCT is proposed by combining transverse and vertical partitions with square holes. Further, the accuracy, reliability and advantages of the prediction expression for F_{ML} of WMCT are verified through simulation, theoretical derivation and test. It can be concluded as follows:

(1) O UCT's size is $\varphi = 10°$ and $t = 1.29$ mm, while the multi-objective optimization of WMCT shows that it has the optimal energy absorption characteristics when the number of transverse, vertical and holes are all equal to four.

(2) The addition of transverse and vertical partitions can improve the stiffness of the WMCT, while the F_{IPL} can be reduced by uniformly opening holes in the tube wall. Therefore, compared to the UCT, the F_{IPL} of the WMCT is 23.60% smaller, while the SEA and EA increase by 70.06% and 90.66%, respectively.

(3) It is proved that the prediction expression for F_{ML} of WMCT has good universal applicability through more simulation data. Relative errors of the three test results is less than 10%, which shows that the prediction expression is reliable and effective. At the same time, it is further verified that WMCT has better energy absorption characteristics than UCT.

Acknowledgement: Special thanks are also given to Engineer Li Huang from School of Materials and Science Engineering, Fujian University of Technology, who provided guidance on the use of the equipment during the experiment, and Jinquan Guo from the School of Mechanical and Automation Engineering, Fuzhou University, who provided comments during the writing.

Funding Statement: This work was supported by the Natural Science Foundation of Fujian Province (grant number 2021J011050, https://kjt.fujian.gov.cn/xxgk/ghjh/202110/t20211008_5701311.htm) (accessed on 08 December 2024) and the Open Fund of Fujian Key Laboratory of Force Measurement (Fujian Academy of Metrology, grant number LZSYS202303, http://www.fjlab.org.cn/showInfoFrame.do?id=216&branch=zxinfo) (accessed on 08 December 2024) with Tieping Wei as the recipient of the funding.

Author Contributions: The authors confirm contribution to the paper as follows: study conception and design: Tieping Wei, Xiang Lin; data collection: Chao Kou, Shoujin Zeng; analysis and interpretation of results: Tieping Wei, Xiang Lin; draft manuscript preparation: Tieping Wei, Xiang Lin; Xingyang Zhou. All authors reviewed the results and approved the final version of the manuscript.

Availability of Data and Materials: The data that support the findings of this study are available from the corresponding author, Tieping Wei, upon reasonable request.

Ethics Approval: Not applicable.

Conflicts of Interest: The authors declare no conflicts of interest to report regarding the present study.

References

1. Deng X, Liu W. Multi-objective optimization of thin-walled sandwich tubes with lateral corrugated tubes in the middle for energy absorption. Thin-Walled Struct. 2019 Apr;137(1/2/3):303–17. doi:10.1016/j.tws.2018.12.040.

2. Asanjarani A, Mahdian A, Dibajian SH. Comparative analysis of energy absorption behavior of tapered and grooved thin-walled tubes with the various geometry of the cross section. Mech Adv Mater Struct. 2020 Apr;27(8):633–44. doi:10.1080/15376494.2018.1488311.
3. Zhao X, Zhu G, Zhou C, Yu Q. Crashworthiness analysis and design of composite tapered tubes under multiple load cases. Compos Struct. 2019 Aug;222(1):110920. doi:10.1016/j.compstruct.2019.110920.
4. Wang Z, Jin X, Li Q, Sun G. On crashworthiness design of hybrid metal-composite structures. Int J Mech Sci. 2020 Apr;171(1):105380. doi:10.1016/j.ijmecsci.2019.105380.
5. Yang H, Lei H, Lu G, Zhang Z, Li X, Liu Y. Energy absorption and failure pattern of hybrid composite tubes under quasi-static axial compression. Compos Part B: Eng. 2020 Oct;198:108217. doi:10.1016/j.compositesb.2020.108217.
6. Xia L, Wang R, Chen G, Asemi K, Tounsi A. The finite element method for dynamics of FG porous truncated conical panels reinforced with graphene platelets based on the 3-D elasticity. Adv Nano Res. 2023;14(4):375–89. doi:10.12989/anr.2023.14.4.375.
7. Duan L, Hong W, Xu W, Du Z, Shi L, Xu D. Study on energy absorption capacity of thin-walled structures with variable cross-section shapes. Aust J Mech Eng. 2024 Jan;22(1):161–78. doi:10.1080/14484846.2022.2069920.
8. Guler MA, Cerit ME, Bayram B, Gerçeker B, Karakaya E. The effect of geometrical parameters on the energy absorption characteristics of thin-walled structures under axial impact loading. Int J Crashworthiness. 2010 Oct;15(4):377–90. doi:10.1080/13588260903488750.
9. Xing J, Xu P, Yao S, Zhao H, Zhao Z, Wang Z. Study on the layout strategy of diaphragms to enhance the energy absorption of thin-walled square tubes. Structures. 2021 Feb;29:294–304. doi:10.1016/j.istruc.2020.11.024.
10. Qiu N, Gao Y, Fang J, Feng Z, Sun G, Li Q. Crashworthiness analysis and design of multi-cell hexagonal columns under multiple loading cases. Finite Elem Anal Des. 2015 Oct;104:89–101. doi:10.1016/j.finel.2015.06.004.
11. Kathiresan M. Effects of cutout and impact loading condition on crashworthiness characteristics of conical frusta. Int J Crashworthiness. 2022 Jul;27(4):1046–66. doi:10.1080/13588265.2021.1903280.
12. Wang Z, Liu Z, Tao C, Liang X. Crashworthiness and optimization design of additive manufacturing double gradient lattice enhanced thin-walled tubes under dynamic impact loading. Eng Fail Anal. 2024 Dec;166(1):108865. doi:10.1016/j.engfailanal.2024.108865.
13. Gao G, Dong H, Tian H. Collision performance of square tubes with diaphragms. Thin-Walled Struct. 2014 Jul;80(1):167–77. doi:10.1016/j.tws.2014.03.007.
14. Xu P, Chen K, Xing J, Qu QY, Yao SG. Energy absorption characteristics and multi-objective optimization of thin-walled square tubes with single cones and internal plates. J Railway Sci Eng. 2019;16(1):185–91. doi:10.19713/j.cnki.43-1423/u.2019.01.025.
15. Jusuf A, Dirgantara T, Gunawan L, Putra IS. Crashworthiness analysis of multi-cell prismatic structures. Int J Impact Eng. 2015 Apr;78(2):34–50. doi:10.1016/j.ijimpeng.2014.11.011.
16. Zhang X, Zhang H. Some problems on the axial crushing of multi-cells. Int J Mech Sci. 2015 Nov;103(9):30–9. doi:10.1016/j.ijmecsci.2015.08.026.
17. Chen J, Liang X, Xu P, Yao S. Crashworthiness analysis and multi-objective optimisation of multi-cell windowed structures under dynamic impact loading. Shock Vib. 2022;2022(1):2263308. doi:10.1155/2022/2263308.
18. Chen S, Zhang M, Zhao L, Wei T. Calculation of the initial peak loads on thin-walled circular tubes with internal and external staggered grooves under low-velocity impacts. Revista Internacional de Métodos Numéricos para Cálculo y Diseño en Ingeniería. 2024 May;40(2). doi:10.23967/j.rimni.2024.05.006.
19. Zhou CH, Ming SZ, Xia CX, Wang B, Bi XJ, Hao P, et al. The energy absorption of rectangular and slotted windowed tubes under axial crushing. Int J Mech Sci. 2018 Jun;141:89–100. doi:10.1016/j.ijmecsci.2018.03.036.

20. Song J, Chen Y, Lu G. Light-weight thin-walled structures with patterned windows under axial crushing. Int J Mech Sci. 2013 Jan;66:239–48. doi:10.1016/j.ijmecsci.2012.11.014.
21. Song J, Guo F. A comparative study on the windowed and multi-cell square tubes under axial and oblique loading. Thin-Walled Struct. 2013 May;66:9–14. doi:10.1016/j.tws.2013.02.002.
22. Feli S, Makhsousse E, Jafari SS. Dynamic progressive buckling of thin-wall grooved conical tubes under impact loading. Int J Crashworthiness. 2020 Mar;25(2):220–9. doi:10.1080/13588265.2019.1573476.
23. Nikkhah H, Guo F, Chew Y, Bai J, Song J, Wang P. The effect of different shapes of holes on the crushing characteristics of aluminum square windowed tubes under dynamic axial loading. Thin-Walled Struct. 2017 Oct;119:412–20. doi:10.1016/j.tws.2017.06.036.
24. Gupta NK, Gupta SK. Effect of annealing, size and cut-outs on axial collapse behaviour of circular tubes. Int J Mech Sci. 1993 Jul;35(7):597–613. doi:10.1016/0020-7403(93)90004-E.
25. Gupta NK. Some aspects of axial collapse of cylindrical thin-walled tubes. Thin-Walled Struct. 1998 Sep;32(1):111–26. doi:10.1016/S0263-8231(98)00029-9.
26. Babaei M, Kiarasi F, Asemi K. Torsional buckling response of FG porous thick truncated conical shell panels reinforced by GPLs supporting on Winkler elastic foundation. Mech Based Des Struct Mach. 2024 Jun;52(6):3552–81. doi:10.1080/15397734.2023.2205488.
27. Postlethwaite HE, Mills B. Use of collapsible structural elements as impact isolators, with special references to automotive applications. J Strain Anal. 1970 Jan;5(1):58–73. doi:10.1243/03093247V051058.
28. Alexander JM. An approximate analysis of the collapse of thin cylindrical shells under axial loading. Q J Mech Appl Math. 1960;13(1):10–5. doi:10.1093/qjmam/13.1.10.
29. Mamalis AG, Manolakos DE, Viegelahn GL, Johnson W. The modelling of the progressive extensible plastic collapse of thin-wall shells. Int J Mech Sci. 1988 Jan;30(3):249–61. doi:10.1016/0020-7403(88)90058-6.
30. Zhang X, Cheng G, Zhang H. Theoretical prediction and numerical simulation of multi-cell square thin-walled structures. Thin-Walled Struct. 2006 Nov;44(11):1185–91. doi:10.1016/j.tws.2006.09.002.
31. Wei TP, Zhou XY, Guo JQ, Zeng SJ, Ye JH, Yang XX. Numerical analysis and theoretical studies of axial compression behavior of A6061 thin-walled conical tubes. China Mech Eng. 2022 Aug;33(14):1725–33, 1750. doi:10.3969/j.issn.1004-132X.2022.14.011.
32. Gang NF, Wang DH, Feng YN, Zhang Q. Numerical simulation and experimental verification of energy absorption performance of PU foam filled CFRP cone tubes. China Mech Eng. 2018 Mar;29(5):609–15. doi:10.3969/j.issn.1004-132X.2018.05.017.
33. Lee S-J, Lee H-A, Yi S-I, Kim D-S, Yang HW, Park G-J. Design flow for the crash box in a vehicle to maximize energy absorption. Proc Inst Mech Eng Part D: J Automobile Eng. 2013 Feb;227(2):179–200. doi:10.1177/0954407012451545.
34. Mamalis AG, Manolakos DE, Ioannidis MB, Kostazos PK. Numerical simulation of thin-walled metallic circular frusta subjected to axial loading. Int J Crashworthines. 2005 May;10(5):505–13. doi:10.1533/ijcr.2005.0365.
35. Sun G, Xu F, Li G, Li Q. Crashing analysis and multiobjective optimization for thin-walled structures with functionally graded thickness. Int J Impact Eng. 2014 Feb;64:62–74. doi:10.1016/j.ijimpeng.2013.10.004.